Semiconductor Physics, Quantum Electronics & Optoelectronics, 2017. V. 20, N 1. P. 55-63.
doi: https://doi.org/10.15407/spqeo20.01.055

PACS 73.61.-r, 78.20.-e, 81.15.-z

An original way to obtain porous $Zn_{(1-x)}Mg_xO$ thin films by spray pyrolysis technique

Abdelhakim Mahdjoub[1,*], Abdelaali Hafid[1], Mohammed Salah Aida[2], Abdelhamid Benhaya[3]
[1]*Laboratoire des Matériaux et Structures des Systèmes Electromécaniques et leur Fiabilité (LMSSEF) Université d'Oum El Bouaghi BP 358, Algérie*
**E-mail: abdelmah@yahoo.com*
[2]*Laboratoire des Couches Minces et Interfaces (LCMI), Université de Constantine I, Constantine 25000, Algérie*
[3]*Laboratoire d'Electronique Avancée (LEA), Université de Batna, Batna 05000, Algérie*

Abstract. $Zn_{(1-x)}Mg_xO$ thin films with various concentrations of magnesium were deposited using the spray pyrolysis method. The transmittance spectra recorded for all films exhibit maxima exceeding 90%. The band gap energy of the films with wurtzite structure increases from 3.22 up to 3.60 eV by incorporating Mg into ZnO. However, when the atomic ratio of Mg exceeded 0.4, a second crystalline phase (assigned to cubic MgO) became discernable in XRD patterns, a compressive strain was observed in the wurtzite lattice, and crystallite sizes decreased significantly. In accordance with these observations, finer grains with a pronounced columnar growth were observed in 3D AFM representations and the surface roughness decreases significantly. Finally, selective etching in water yields to porous films with a great surface-to-volume ratio, a lower refractive index and a better light transmission. These porous films with tunable band gap seem to be excellent candidates to various interesting applications.

Keywords: zinc oxide, magnesium, thin films, transmittance, porosity.

Manuscript received 22.11.16; revised version received 01.02.17; accepted for publication 01.03.17; published online 05.04.17.

1. Introduction

Metallic oxides have many applications in a wide variety of technological areas [1-3]. The most remarkable utility of these materials is by far the TCO (transparent and conducting oxides) application [3-5]. Tin-doped indium oxide (ITO) is certainly the most common TCO, but because of the rarity of indium on earth, ITO remains too expensive. Therefore, researchers try to replace it with more accessible materials. AZO (aluminum doped zinc oxide), IZO (indium doped zinc oxide) and GZO (gallium doped zinc oxide) exhibit interesting optical and electrical properties and seem to be the materials, performances of which are closest to those of ITO [4, 6]. Besides, doped ZnO is usually used as an active material in photodetectors [8, 9] and photocatalysis [10, 11]. For these applications, the active surface affected by the grain size and the film porosity becomes the most important factor improving the device performance [12]. On the other hand, the optical band gap of ZnO can be increased by replacing zinc atoms by magnesium (Mg) [13]. Several works have been published in this area using different deposition methods such as sputtering [14, 15], sol-gel [16], chemical bath deposition [17] and spray pyrolysis [18, 19].

$Zn_{(1-x)}Mg_xO$ would therefore be a tunable band gap semiconductor allowing multiple applications. The aim of this work is to study the magnesium concentration

effect on the optical, structural and morphological properties of $Mg_xZn_{(1-x)}O$ thin films obtained by spray pyrolysis deposition and its impact on potential applications.

2. Experimental procedure

The originality of this work is of having employed a medical nebulizer (Omron CompAir NEC801) for depositing thin films by spray pyrolysis. Beside its low price, the advantage of this apparatus is to help obtain a flux of very fine droplets oriented vertically towards the substrates placed on a thermoregulated heating plate. The substrate holder temperature is maintained at 350 °C allowing a complete decomposition of the precursors. Zinc and magnesium acetates 0.2M aqueous solutions were prepared to serve as precursors for the films deposition. These solutions were mixed in different volume ratios (0:5; 1:4; 2:3, 3:2; 4:1 and 5:0) to obtain $Zn_{(1-x)}Mg_xO$ alloys ranging from ZnO to MgO. The total dissolution of the precursors in the solvent is therefore essential for obtaining the right chemical composition. A clear solution without any precipitate is then sought. If this procedure is scrupulously respected, the chemical composition of the deposited film will correspond perfectly to the chosen proportions of precursors.

Two similar sets of films were deposited on silica and silicon substrates to allow a larger variety of characterization. Morphology of the deposited layers was observed using atomic force microscopy with the A100 model of APEResearch. The crystalline structure was explored by X-ray diffraction (EQ-MD10 diffractometer with a Cu-tube). Analysis of transmittance and ellipsometric spectra, recorded using respectively JASCO 630 spectrophotometer and Angstrom-Advanced spectroscopic ellipsometer, allows the study of the optical properties of the deposited films.

3. Results and discussion

3.1. Effect of magnesium concentration on the $Zn_{(1-x)}Mg_xO$ structure

XRD patterns recorded between 20° and 75° on the six $Zn_{(1-x)}Mg_xO$ thin films deposited on silicon substrates are shown in Fig. 1. The spray pyrolysis technique performed at 350 °C favors crystallization of the deposited materials. Furthermore, the silicon substrates were used to avoid the background noise due to amorphous materials. Good quality diffractograms were obtained in comparison to similar studies carried out on $Zn_{(1-x)}Mg_xO$ thin films [17, 20]. For atomic magnesium ratios x less than 0.4, the XRD patterns show exclusively characteristic peaks inherent to the ZnO wurtzite structure [JCPDS File No.36-1451]. For x higher than 0.4, the characteristic peaks of MgO cubic structure clearly appear on the XRD patterns and become dominant when approaching pure MgO [JCPDS File No.74-1225]. Note that 40% of Mg failed to bring out an MgO phase accompanying the wurtzite structure, while 20% Zn impose their presence in the cubic structure of MgO. The incorporation of Mg (Mg^{2+} slightly smaller than Zn^{2+} [20]) in ZnO is much larger than that of Zn in MgO. Choopun *et al.* reported that the solid solubility of MgO in ZnO for thin-film samples did not exceed 33% [21]. Above this concentration, MgO segregates from wurtzite lattice in cubic phase. This is in agreement with our results, if it is assumed that for $x = 0.4$ the MgO cubic phase was not sufficient to be observed within the detection limit of our measurement. In Fig. 1, we notice a slight shift of the strongest peak (002) from 34.62° for ZnO to 34.98° in the case of $Zn_{0.4}Mg_{0.6}O$ alloy, indicating a diminution in the hexagonal lattice parameter c. This behavior has been observed by Maemoto *et al.* [22].

The broadening of the diffraction peaks, directly related to the crystallite size and lattice strain, was analyzed using the Williamson–Hall (W-H) method [23], being based on the following equation:

$$\frac{\beta\cos\theta}{\lambda} = \frac{0.9}{d} + \frac{4\varepsilon\sin\theta}{\lambda}, \qquad (1)$$

where $\beta = \sqrt{\beta_m^2 - \beta_0^2}$ represents the peak broadening after removing the instrumental contribution (β_0 = 0.001 radians), (β_m – measured full width at half maximum (in radians), ε – lattice strain, θ – Bragg angle, d – average crystallite size, and λ – wavelength of X-rays.

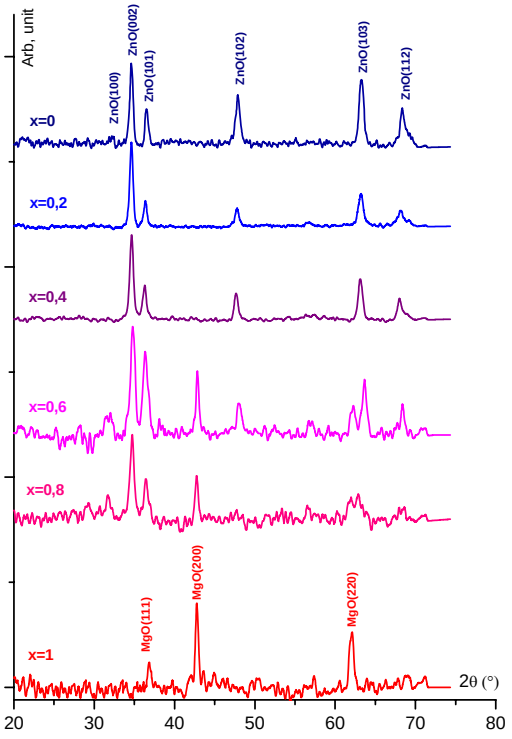

Fig. 1. XRD patterns of $Zn_{(1-x)}Mg_xO$ thin films deposited on silicon substrates for x = 0, 0.2, 0.4, 0.6, 0.8, 1.

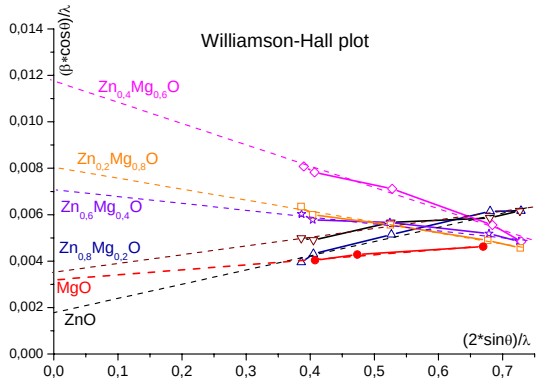

Fig. 2. Williamson–Hall plots of $Zn_{(1-x)}Mg_xO$ for wurtzite and MgO cubic phases.

Using the W-H plot, the lattice strain and crystallite sizes were calculated respectively from the slope of the linear fit and the y-intercept (Fig. 2). This analysis was applied to (002), (101), (102), (103), (112) corresponding peaks of wurtzite phase as well as those corresponding to (111), (200) and (220) planes of the MgO cubic phase.

The results of W-H analysis are summarized in Table 1 for the wurtzite phase and Table 2 for MgO. As can be seen, increasing the Mg concentration (for $x < 0.6$) is accompanied with wurtzite crystallite sizes and lattice strain decrease (Fig. 3). Furthermore, for x between 0.4 and 0.8, when the cubic phase appeared beside the hexagonal one, the slope of W-H plots was reverted, and the strain became compressive. When only MgO was deposited, the crystallite size increased to 27.9 nm, and the strain became tensile again (Table 2).

These results demonstrate that the presence of both hexagonal and cubic phases at the same time induces compression in the lattice of each phase and hinders the growth of larger particles. Similar correlation between the compressive strain and crystallite sizes was reported by Cheong *et al*. in their study of TiO_2 thin films [24]. Reyes-Rojas *et al.* reported that the addition of ZrO_2 and Y_2O_3 increased the compressive strain in alumina polycrystal and affected the grains growth [25].

3.2. Morphological aspect

Nanoscale 3D representation of the surface recorded by AFM for the six samples prepared on silicon substrates is shown in Fig. 4. The grains have a rounded shape with a columnar growth. The size of MgO grains (exceeding 260 nm) is greater than that of ZnO (around 190 nm). For $Zn_{(1-x)}Mg_xO$ alloys, the grain size is slightly smaller than that of ZnO (between 150 and 180 nm) as long as the cubic phase does not appear ($x < 0.4$). When the cubic phase becomes important, finer grains (less than 100 nm) with a pronounced columnar growth are observed, and therefore the surface roughness decreases significantly (RMS indicated in Table 3). The simultaneous presence of two competitive phases (wurtzite and cubic) favors a growth of fine columns resulting in a low surface roughness. Similar behavior was observed by Tsay *et al*. in their work [20].

These observations clearly illustrated in Fig. 5, confirm the tendency emerging from the XRD analysis. However, it should be noticed that the grains size estimated by AFM is much greater than that of the crystallites calculated from XRD patterns. Presumably, each grain observed by AFM contains several nanocrystallites revealed by XRD.

Table 1. Williamson–Hall XRD analysis of the wurtzite phase.

(hkl)	Atom. ratio	0	0.2	0.4	0.6	0.8
(002)	θ (deg.)	17.31	17.31	17.33	17.49	17.29
	β_m (deg.)	0.369	0.468	0.563	0.752	0.593
(101)	θ (deg.)	18.185	18.185	18.14	18.27	18.13
	β_m (deg.)	0.409	0.453	0.543	0.731	0.563
(102)	θ (deg.)	23.94	23.9	23.83	24.00	23.87
	β_m (deg.)	0.503	0.553	0.553	0.692	0.543
(103)	θ (deg.)	31.63	31.61	31.55	31.82	31.44
	β_m (deg.)	0.642	0.612	0.543	0.582	0.513
(110)	θ (deg.)	34.17	34.08	34.00	34.19	34.10
	β_m (deg.)	0.652	0.662	0.523	0.523	0.493
Crystallites size (nm)		54.8	25.3	12.6	7.8	11.2
Lattice strain (10^{-3})		3.2	1.8	–1.5	–4.5	–2.4

Table 2. Williamson–Hall XRD analysis of the MgO cubic phase.

Atom. ratio \ (hkl)	(111)	(200)	(220)
θ (deg.)	15.71	21.38	31.06
β_m (deg.)	0.374	0.423	0.483
Crystallites size (nm)		27.9	
Lattice strain (10^{-3})		1.06	

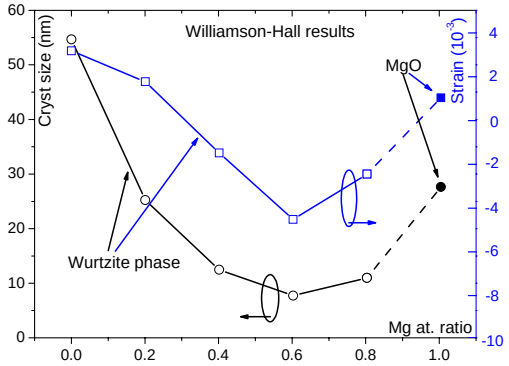

Fig. 3. Crystallite size and lattice strain deduced from the Williamson–Hall plots.

3.3. Optical properties

For transmittance measurements, silica substrates of 1-mm thick were used. Fig. 6 shows the transmittance spectra of $Zn_{(1-x)}Mg_xO$ films for the different values of the atomic ratio *x*, compared to that of the bare silica substrate. Silica is transparent over practically the entire range of wavelengths available by the JASCO 630 spectrophotometer. Interferential fringes are visible on all the spectra recorded for the deposited films. It demonstrates good quality of the deposited films with homogeneous and smooth surface. The fit of the measured spectra by an appropriate mathematical model (detailed out in a previous work [26]) allows determining the thicknesses indicated in Fig. 6.

The transmittance maxima recorded on all the films are very close to the transmittance of silica (maximum value is 93.5%). MgO is practically transparent across the measured spectrum, whereas ZnO has an absorption edge around 380 nm corresponding to a band gap energy of 3.22 eV (in good agreement with the published values) [27]. For $Zn_{(1-x)}Mg_xO$ alloys with atomic ratio *x* between 0.2 and 0.4, a single absorption edge dominates.

The band gap energy increases up to 3.54 eV in agreement with the results reported by Tsay *et al*. [20]. When the atomic ratio exceeds this value (*x* between 0.6 and 0.8), two optical transitions appear, corresponding to the two crystalline phases (wurtzite and cubic) revealed by XRD. The lowest transition situated at 3.6 eV corresponds to wurtzite phase. The second one approaches that of the MgO thin films, estimated by Badar *et al*. at 5.5 eV [28]. The transmittance spectra recorded for the samples with columnar growth (for x = 0.6 or 0.8) exhibit larger amplitude fringes probably due to the diminution of surface roughness [26].

For ellipsometric measurements, monocrystalline silicon substrates were used. Fig. 7 shows the ellipsometric spectra of $Zn_{(1-x)}Mg_xO$ films for the different values of the atomic ratio *x*. The ellipsometric angles ψ and Δ are plotted as functions of the incident photon energy hν. In the part of the spectrum where the films are transparent, interferential fringes can be observed. However, in the absorption area, the interferential fringes disappear [29]. For $Zn_{(1-x)}Mg_xO$ alloys with atomic ratio *x* between 0.2 and 0.4, the limit between the two areas is clearly discernible, and thus the values of the band gap energy can be estimated. These values are indicated in Table 4 and correspond well to those previously calculated using the results of UV-Vis spectroscopy (see Fig. 8).

When the atomic ratio *x* lies between 0.6 and 0.8, the two crystalline phases (wurtzite and cubic) co-exist, and the transition between the transparency and the absorption areas (situated between 3.5 and 4.5 eV) becomes difficult to discern. This behavior was clearly explained by Choi *et al*. in the previous work [29]. An appropriate mathematical analysis of the ellipsometric spectra would be necessary to separate the two absorption edges [30], but such investigation is not the purpose of this work.

Table 3. Results of the AFM analysis.

Atomic ratio *x*	0	0.2	0.4	0.6	0.8	1
Grain size (nm)	188	176	154	78	97	263
RMS (nm)	18.4	15.1	13.8	5.2	8.6	15.5

Table 4. Band gap energy of $Zn_{(1-x)}Mg_xO$.

Atomic ratio *x*	0	0.2	0.4	0.6	0.8	1
Optical gap (eV) (from transmittance)	3.22	3.39	3.53	3.58	3.60	5.42
Optical gap (eV) (from ellipsometry)	3.26	3.36	3.54	–	–	–

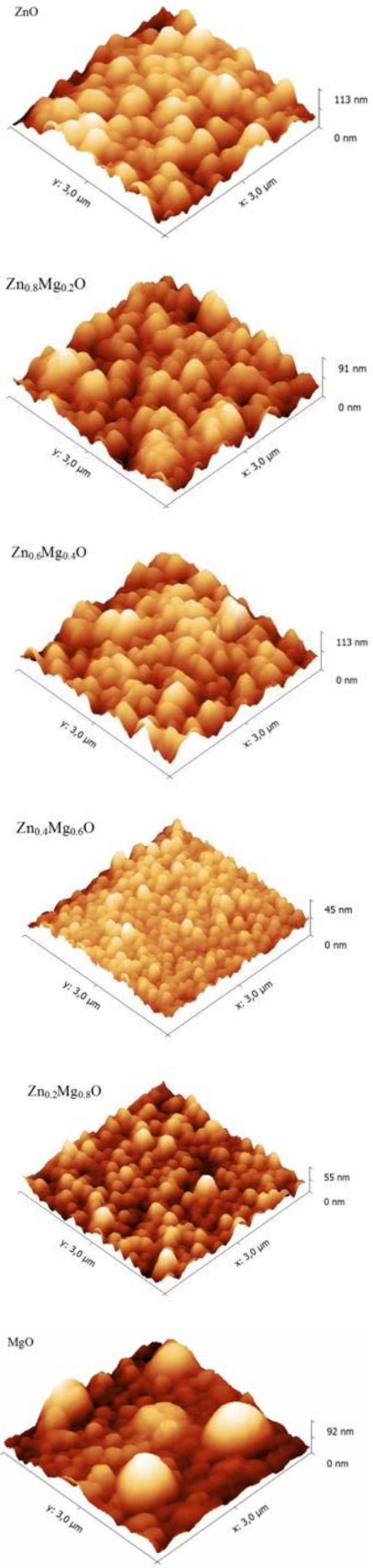

Fig. 4. AFM 3D representation of $Zn_{(1-x)}Mg_xO$ thin films deposited on silicon substrates

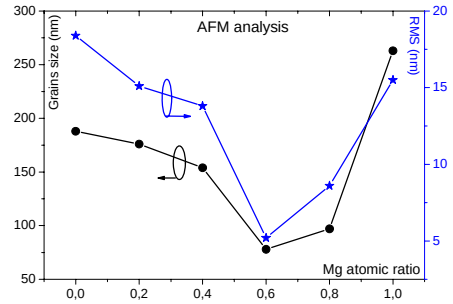

Fig. 5. Grains size and RMS deduced from AFM.

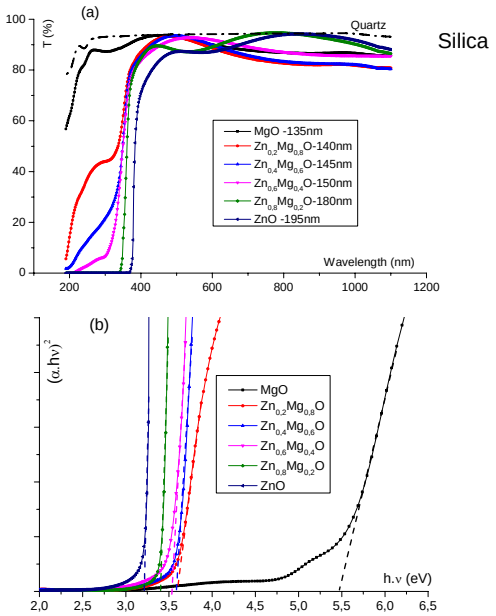

Fig. 6. Transmittances of $Zn_{(1-x)}Mg_xO$ thin films deposited on silica (a) and band gap energy determination (b).

3.4. Porous $Zn_{(1-x)}Mg_xO$ thin films

Based on the above results, especially the coexistence of two crystalline phases (wurtzite close to ZnO and cubic close to MgO), and knowing that MgO, contrary to ZnO, is soluble in water [31], the idea of making a porous material by a selective etching becames evident. $Zn_{0.2}Mg_{0.8}O$ samples prepared on silica and silicon substrates were etched in deionized water at 60 °C for two hours. The changes introduced to the surface morphology were observed by AFM and reported in 3D representation (Fig. 9).

Morphology was totally changed and presented growth in oriented column-forms. The mean grain size estimated by AFM decreased drastically from 97 nm (indicated in Table 3) down to 22 nm. The deposited films then became nanoporous and presented a greater surface-to-volume ratio. This behavior can be explained by dissolution of the cubic phase MgO surrounding columns of wurtzite phase. The small size of the grains observed by AFM after treatment approaches the XRD crystallites size reported in Table 1.

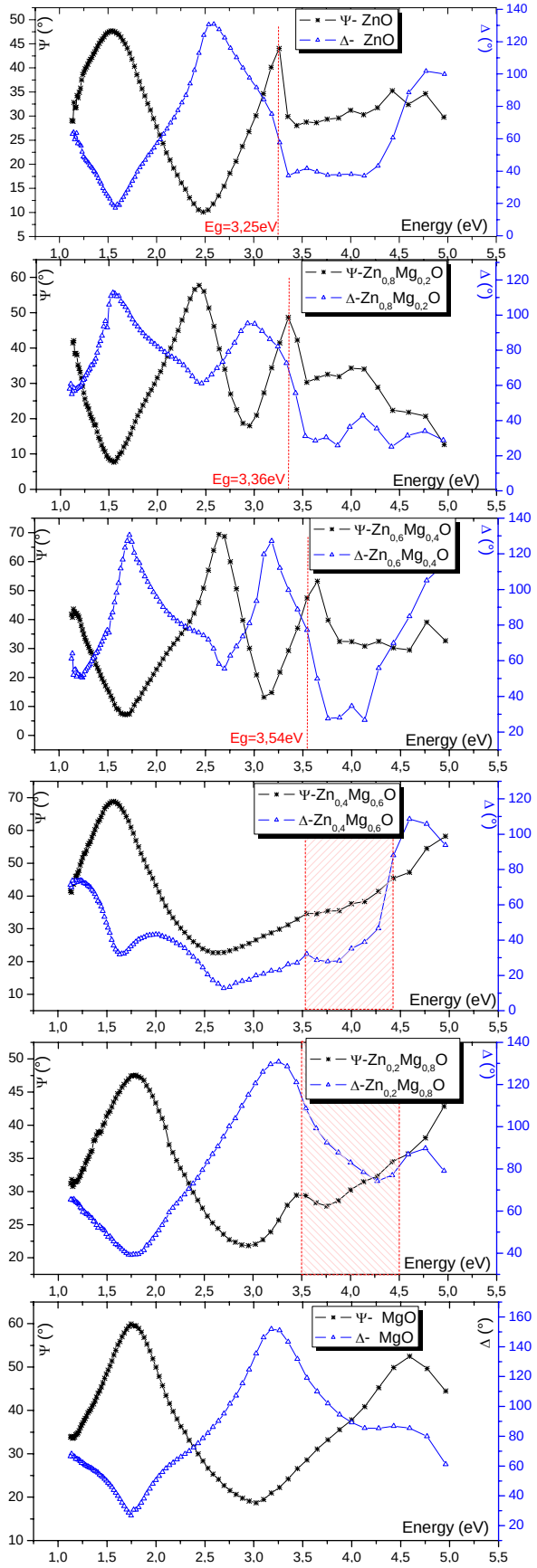

Fig. 7. Ellipsometric spectra of $Zn_{(1-x)}Mg_xO$ thin films.

Transmittance and ellipsometric spectra were recorded for optical study. The film porosity causes diminution of the refractive index, which increases the transmittance of the films in the transparent part of the spectrum (Fig. 10). Reduction in the interferential fringes amplitude, resulting from a lower refractive index [26], maintains the transmittance at a higher level. In contrast, in the absorption area, the transmittance is lower after water etching. The optical confinement in the pores and the multiple reflections caused by the textured surface amplify the absorption effect decreasing the transmitted light.

The ellipsometric spectra recorded before and after etching (Fig. 11) show a clear difference. The interferential fringes were shifted and had a greater amplitude. An appropriate mathematical analysis [30] of these spectra allows determining the refractive index dispersion in the transparent area highlighting the etching effect, as shown in Fig. 12. The ellipsometric results confirm the diminution of the film refractive index induced by the porosity resulting from the water etching.

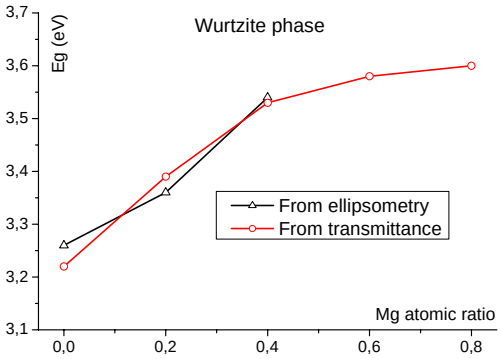

Fig. 8. Band gap energy determinated from transmittance and ellipsometric spectra.

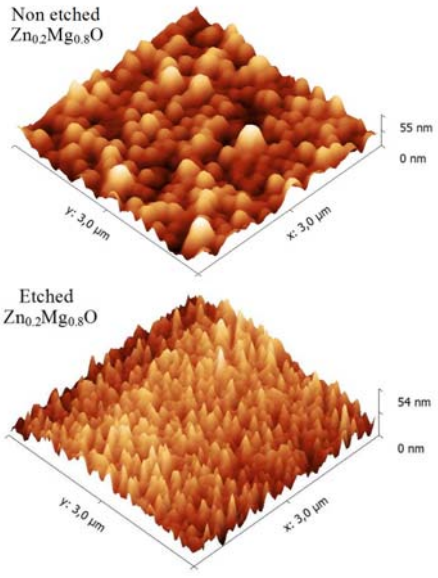

Fig. 9. AFM 3D representation of $Zn_{0.2}Mg_{0.8}O$ thin films before and after etching in water.

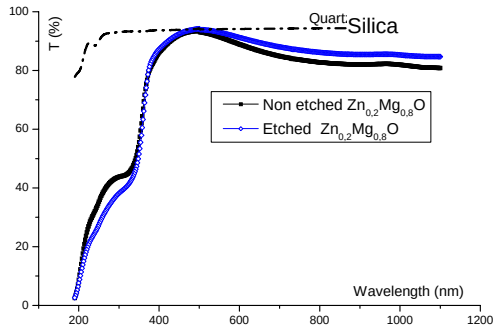

Fig. 10. Transmittance of $Zn_{0.2}Mg_{0.8}O$ thin films before and after etching in water.

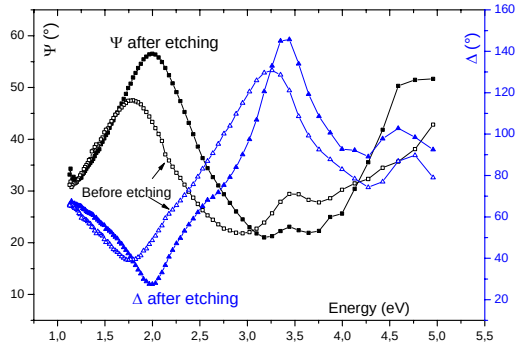

Fig. 11. Ellipsometric spectra of $Zn_{0.2}Mg_{0.8}O$ thin films before and after etching in water.

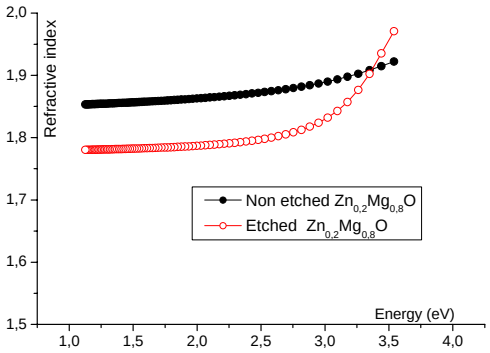

Fig. 12. Refractive index of $Zn_{0.2}Mg_{0.8}O$ thin films before and after etching in water.

This study highlights the great technological potential of $Zn_{(1-x)}Mg_xO$ nanoporous films, with tunable band gap enabling several optoelectronic applications [30], high transparency for photovoltaic applications [31] and a large active surface essential for chemical sensors [32] and photocatalysis [33].

4. Conclusion

Good quality $Zn_{(1-x)}Mg_xO$ thin films with tunable band gap were deposited by simple spray pyrolysis method. The transmittance maxima recorded on all films exceed 90%. An important increase of the band gap energy (from 3.22 to 3.6 eV) is possible while maintaining the wurtzite-like phase (for atomic ratio less than 0.4). If the atomic ratio of Mg exceeds this value, two crystalline phases (wurtzite and cubic) grow in competition resulting in a compressive lattice strain. Therefore, finer grains with a pronounced columnar growth are observed, and the surface roughness decreases significantly. A simple etching in water yields to nanoporous films, with a great surface-to-volume ratio, a lower refractive index and a better light transmission. These properties might be interesting for various applications.

Acknowledgements

We would like to thank researchers and technicians of LCAM-OEB and the Faculty of Chemistry (USTHB) for their technical assistance in accomplishing this work.

References

1. Shriram R. *Thin Film Metal-Oxides; Fundamentals and Applications in Electronics and Energy*. Springer, 2010.
2. Markus N. and Nicola P. *Metal Oxide Nanoparticles in Organic Solvents; Synthesis, Formation, Assembly and Application, Engineering Materials and Processes*. Springer, 2009.
3. Willander M., Zhao Q.X., Hu Q.-H., Klason P., Kuzmin V., Al-Hilli S.M., Nur O., Lozovik Y.E. Fundamentals and properties of zinc oxide nanostructures: Optical and sensing applications. *Superlatt. Microstruct*. 2008. **43**. P. 352–361.
4. Szyszka B., Dewald W., Gurram S.K., Pflug A., Schulz C., Siemers M., Sittinger V., Ulrich S. Recent developments in the field of transparent conductive oxide films for spectral selective coatings, electronics and photovoltaics. *Current Appl. Phys*. 2012. **12**. P. S2–S11.
5. Ginley D.S. *Applications of Transparent Conductors to Solar Energy and Energy Efficiency.* Handbook of Transparent Conductors. Springer, 2011. P. 353–423.
6. Liu H., Avrutin V., Izyumskaya N., Özgür Ü., Morkoç H. Transparent conducting oxides for electrode applications in light emitting and absorbing devices. *Superlatt. Microstruct.* 2010. **48**. P. 458–484.
7. Kwak D.J., Moon B.H., Lee D.K., Park C.S. and Sung Y.M. Comparison of transparent conductive indium tin oxide, titanium-doped indium oxide, and fluorine-doped tin oxide films for dye-sensitized solar cell application. *J. Electr. Eng. and Technol.* 2011. **6**. P. 684–687.

8. Liu C.Y., Xu H.Y., Sun Y., Zhang C., Ma J.G., Liu Y.C. Ultraviolet electroluminescence from Au/MgO/$Mg_xZn_{1-x}O$ heterojunction diodes and the observation of Zn-rich cluster emission. *J. Lumin.* 2014. **148**. P. 116–120.
9. Schoenfeld W.V., Wei M., Boutwell R.C., Liu H. High response solar-blind MgZnO photodetectors grown by molecular beam epitaxy. *Proc. SPIE*. 2014. **8987**. Oxide-based Materials and Devices V, 89871P (12 p.).
10. Ivetićan T.B., Dimitrievskaa M.R., Finčurb N.L., Đačanina Lj.R., Gútha I.O., Abramovićb B.F., Lukić-Petrovića S.R. Effect of annealing temperature on structural and optical properties of Mg-doped ZnO nanoparticles and their photocatalytic efficiency in alprazolam degradation. *Ceramics Intern*. 2014. **40**. P. 1545–1552.
11. Zhou Z., Shang F., Pan G., Wang F., Liu C., Gong W., Zi Z., Wei Y., Lu J., Chen X. Enhanced photocatalytic activity of $Mg_{0.05}Zn_{0.95}O$ thin films prepared by sol–gel method through a cycle. *J. Mater. Sci.: Mater. Electron.* 2014. **25**. P. 2053–2059.
12. Shang C., Thimont Y., Barnabé A., Presmanes L., Pasquet I., Tailhades P. Detailed microstructure analysis of as-deposited and etched porous ZnO films. *Appl. Surf. Sci*. 2015. **344**. P. 242–248.
13. Sharma M., Jeevanandam P. Magnesium doping in hierarchical ZnO nanostructures and studies on optical properties. *Superlatt. Microstruct.* 2012. **52**. P. 1083–1092.
14. Hsueh K.P., Cheng Y.C., Lin W.Y., Chiu H.C., Huang Y.P., Chi G.C., Liu W.S. Physical properties of Al-doped MgZnO film grown by RF magnetron sputtering using ZnO/MgO/Al_2O_3 target. *Thin Film Solar Technology* III, 81100X, doi:10.1117/12.891269 (2011).
15. Karthick K., Vijayalakshmi K. Influence of Mg doping on the properties of ZnO films prepared on c-cut sapphire by sputtering. *Superlatt. Microstruct*. 2014. **67**. P. 172–180.
16. Sengupta J., Ahmed A., Labar R. Structural and optical properties of post annealed Mg doped ZnO thin films deposited by the sol-gel method. *Mater. Lett*. 2013. **109**. P. 265–268.
17. Vijayalakshmi K., Renitta A., Karthick K. Growth of high quality ZnO:Mg films on ITO coated glass substrates for enhanced H_2 sensing. *Ceramics Intern*. 2014. **40**. P. 6171–6177.
18. Yoshino K., Oyama S., Yoneta M. Structural, optical and electrical characterization of undoped ZnMgO film grown by spray pyrolysis method. *J. Mater. Sci.: Mater. Electron*. 2008. **19**. P. 203–209.
19. Hoggas K., Nouveau C., Djelloul A., Bououdina M. Structural, microstructural, and optical properties of $Zn_{1-x}Mg_xO$ thin films grown onto glass substrate by ultrasonic spray pyrolysis. *Appl. Phys. A.* 2015. **120**. P. 745–755.
20. Tsay C.Y., Wang M.C., and Chiang S.C. Effects of Mg additions on microstructure and optical properties of Sol-Gel derived ZnO thin films. *Mater. Trans*. 2008. **49**. P. 1186–1191.
21. Choopun S., Vispute R.D., Yang W., Sharma R.P., Venkatesan T. and Shen H. Realization of band gap above 5.0 eV in metastable cubic-phase $Mg_xZn_{1-x}O$ alloy films. *Appl. Phys. Lett*. 2002. **80**. P. 1529–1531.Maemoto T., Ichiba N., Ishii H., Sasa S., Inoue M. Structural and optical properties of ZnMgO thin films grown by pulsed laser deposition using ZnO-MgO multiple targets. *J. Phys.: Conf. Series*. 2007. **59**. P. 670–673.Mallika A.N., Reddy A. Ramachandra, Babu K. Sowri, Sujatha C., Reddy K. Venugopal Structural and photoluminescence properties of Mg substituted ZnO nanoparticles. *Opt. Mater*. 2014. **36**. P. 879–884.
24. Cheong Y.L., Yam F.K., Chn I.K., Hassan Z. X-ray analysis of nanoporous TiO_2 synthesized by electrochemical anodization, *Superlatt. Microstruct*. 2013. **64**. P. 37–43.
25. Reyes-Rojasa A., Esparza-Poncea H., De la Torreb S.D., Torres-Moyea E. Compressive strain-dependent bending strength property of Al_2O_3–ZrO_2, (1.5 mol% Y_2O_3) composites performance by HIP. *Mater. Chem. Phys.* 2009. **114**. P. 756–762.
26. Mahdjoub A., Moualkia H., Remache L., Hafid A. Analyse des spectres de transmittance des couches minces par une modélisation mathématique appropriée. *Rev. Alg. Phys.* 2015. **2**. P. 30–37.
27. Ü. Özgür, I. Alivov Ya, C. Liu, A. Teke, M. A Reshchikov, S. Do□an, V. Avrutin, S.J. Cho, H. Morkoç, A comprehensive review of ZnO materials and devices. *J. Appl. Phys.* 2005. **98**, P. 041301–041301.
28. Badar N., Chayed N.F., Rusdi R., Kamarudin N. and Kamarulzaman N. Band gap energies of magnesium oxide nanomaterials synthesized by the Sol-Gel method. *Adv. Mater. Res.* 2012. **545**, P. 157–160.
29. Choi W.S., Yoon J.G. Optical characterization of band gap graded ZnMgO films. *Solid State Communs*. 2012. 152. P. 345–348.
30. Benzitouni S., Mahdjoub A., Zaabat M. Spectroscopic ellipsometry characterization of thin films deposited on silicon substrate. *J. New Technol. Mater*. 2014. **04**. P. 138–142.
31. Ropp R.C. *Encyclopedia of the Alkaline Earth Compounds*. Elsevier, 2013. P. 108.
32. Su S.C., Lu Y.M., Xing G.Z., Wu T. Spontaneous and stimulated emission of ZnO/$Zn_{0.85}Mg_{0.15}O$ asymmetric double quantum wells. *Superlatt. Microstruct.* 2010. **48**. P. 485–490.
33. Jiang J., Wang J., Tang Y. Mesoporous F-doped ZnO prism arrays with significantly enhanced photovoltaic performance for dye-sensitized solar cells. *J. Power Sources*. 2011. **196**. P. 10518–10525.
34. Cui J., Sun J., Liu X., Li J., Ma X., Chen T. Fabrication of hierarchical flower-like porous ZnO

nanostructures from layered $ZnC_2O_4 \cdot 3Zn(OH)_2$ and gas sensing properties. *Appl. Surf. Sci.* 2014. **308**. P. 17–23.

35. Chen Y., Zhang L., Ning L., Zhang C., Zhao H., Liu B., Yang H. Superior photocatalytic activity of porous wurtzite ZnO nanosheets with exposed {001} facets and a charge separation model between polar (001) and $(00\bar{1})$ surfaces. *Chem. Eng. J.* 2015. **264**. P. 557–564.